Highly selective hydrogenation of CO_2 to propane

Sen Wang,[1] Li Zhang,[1,2] Pengfei Wang,[1] Weiyong Jiao,[1] Zhangfeng Qin,[1] Mei Dong,[1] Jianguo Wang,[1,2] Unni Olsbye,[3] and Weibin Fan[1,*]

[1] *State Key Laboratory of Coal Conversion, Institute of Coal Chemistry, Chinese Academy of Sciences, P.O. Box 165, Taiyuan, Shanxi 030001, PR China*

[2] *University of the Chinese Academy of Sciences, Beijing 100049, PR China*

[3] *Department of Chemistry, Centre for Materials and Nanoscience (SMN), University of Oslo, P.O. Box 1033, Blindern, NO-0315 Oslo, Norway*

[*] *Corresponding author.* Tel.: +86-351-4199009; fax: +86-351-4041153. *E-mail address: fanwb@sxicc.ac.cn (W. Fan)*

Abstract. Highly selective hydrogenation of CO_2 into value-added hydrocarbons, in particular, single product, is of great interest. However, this is a challenge as a result of a very complex reaction network with simultaneous occurrence of numerous forward and reverse tandem and parallel reactions. In this context, a new catalyst system consisting of $GaZrO_x$ and H-SSZ-13 is developed here. At CO_2 conversion of 43.4%, the propane selectivity in hydrocarbons reaches 79.5% along with the butane selectivity of 9.9% and the CO selectivity of only 31.8%. This results in a propane yield as high as 23.6% and a butane yield of 2.9%. This outstanding catalytic performance can be well maintained within 500 h. DFT calculation, isotope-labeled in situ DRIFTS, ^{13}C MAS NMR with pulse-quenched method, GC-MS and various probe experiment results indicate that incorporation of proper amounts of Ga into ZrO_2 promotes methanol formation due to generation of a high concentration of surface oxygen vacancies with moderate adsorption strength of CO_2, and propane and butane are produced through methanol-to-hydrocarbons (MTH) reaction on H-SSZ-13. Unexpectedly, larger numbers of highly strong acid sites in H-SSZ-13 seriously restricts formation of aromatic species at high H_2 pressure. This leads to suppression of the aromatics-based cycle but enhancement of the alkene-based cycle, thus giving far more propene and butene than ethene despite that these olefins are rapidly hydrogenated to corresponding alkanes on the strong acid sites of H-SSZ-13 as a result of their high acid strength.

Keywords: CO_2 hydrogenation, propane, reaction route, precise control, single product

The rapid consumption of fossil resources leads to emission of large amounts of carbon dioxide (CO_2) in atmosphere, which is considered to result in serious environmental problems, such as global warming, ocean acidification and sea level rise, etc.[1–4] Nevertheless, CO_2 is also an economical, nontoxic and abundant carbon resource. Direct conversion of CO_2 into value-added chemicals can not only effectively mitigate the greenhouse effect, but also make the utilization of fossil and biomass become sustainable or carbon-neutral.[5–13]

In this context, CO_2 has been converted into urea, cyclic carbonate and methanol.[14,15] Recently, hydrogenation of CO_2 to liquid fuels and commodity chemicals attracts great research interests,[16,17] and has been tried through thermocatalysis, electrocatalysis and photocatalysis.[18,19] Compared to the latter two catalytic ways, the former one is more potential as it gives far higher yield and is more easily scaled up. Two routes have been employed for thermocatalytic hydrogenation of CO_2. One is Fischer–Tropsch (FT) synthesis route,[20–27] and the other is methanol-intermediate route.[28,29] Compared to the FT synthesis route, the methanol-intermediate route is more interesting because it can effectively break the Anderson–Schulz–Flory (ASF) rule limitation, and give much higher selectivity to target products such as light olefins and aromatics due to significant constraint effect of zeolite component in catalysts. Thus, many efforts have been attempted to development of efficient metal oxide/zeolite composite catalyst for production of methanol on metal oxide and subsequent transformation of methanol into light olefins or aromatics over zeolite.[30–33] Nevertheless, the selectivity to light olefins or aromatics in hydrocarbons generally intermediates between 60% and 87%.[34–43] Further increase of it, in particular, acquirement

of single specific product is still challenging. This is because CO_2 hydrogenation to hydrocarbons involves in many elementary reactions, which leads to simultaneously yielding of numbers of products.

Propane is an important platform molecule, which can be selectively dehydrogenated to propene, and further aromatized to benzene, toluene, xylene and so on with co-production of hydrogen.[44–46] Therefore, direct conversion of CO_2 into propane is not only scientifically important but also practically valuable. Recently, several catalysts, e.g. $CuZnZrO_x$/MeSAPO-34, $CuZnZrO_x$/Pd-Beta, Pd/SiO_2-ZSM-5 and PdZn-ZrO_2/SAPO-34 have been reported to selectively hydrogenate CO_2 to propane and/or liquefied petroleum gas (LPG).[47–51] However, these catalysts show low catalytic stability ($\leq$ 50 h)[47,50] or high selectivity to CO (60 – 80%).[48] It seems that Pd-based catalysts can somewhat lower the CO selectivity along with the increase of the CO_2 conversion,[49,51] but the propane selectivity in hydrocarbons is still lower than 70%. In addition, the use of Pd significantly increases the catalyst preparation cost.

Here, a new catalyst system consisting of $GaZrO_x$ oxide and H-SSZ-13 zeolite is developed, and it shows extraordinary catalytic performance in CO_2 hydrogenation to propane; the selectivity to propane reaches 79.5% along with butane selectivity of 9.9% and CO selectivity of only 31.8% at CO_2 conversion of 43.4%.

Results

Catalytic performance of $GaZrO_x$/H-SSZ-13 composite for hydrogenation of CO_2 to propane. Figure 1(a) and 1(b) shows that ZrO_2/H-SSZ-13 exhibits selectivity to propane of

73.6% and that to LPG (propane + butane) of 81.3% in (hydrocarbons + oxygenates), while CO selectivity of 19.5% at 350 ºC and 3.0 MPa, although its CO_2 conversion is only 5.3%. Interestingly, the CO_2 conversion can be significantly increased along with the propane and LPG selectivities by incorporating Ga in ZrO_2. When the Ga/Zr molar ratio is 0.5, the CO_2 conversion and the propane selectivity rise to 16.3%, and 78.9% respectively at the same reaction conditions (Figure S1). In addition, the LPG selectivity is also elevated to 90.4%, despite that CO selectivity gets to 27.2%. As a result, the propane and LPG yields reach 9.4% and 10.7% respectively (Figure S2). Nonetheless, further increase of the Ga amount decreases both the CO_2 conversion and the selectivities to propane and LPG, but leads to production of more CO. Figure S3 shows that $GaZrO_x(0.5)$ gives the highest methanol space time yield (STY).

The catalytic performance of $GaZrO_x(0.5)$/H-SSZ-13 for hydrogenation of CO_2 to propane is dependent on the H-SSZ-13 acidity. When the Si/Al ratio of H-SSZ-13 is lowered from 22.0 to 6.0, the selectivity of propane and that of LPG increase from 75.8% and 87.6% to 78.9% and 90.4%, although a further decrease of the Si/Al ratio to 3.3 leads to a remarkable reduction of the propane and the LPG selectivities to 40.1% and 42.3% respectively, due to formation of more $C_2^{=}$ – $C_4^{=}$ alkenes (selectivity of 35.4%) (Figure 1(c) and 1(d)). Figure S4(a) shows that the amount and the strength of strong acid sites in H-SSZ-13(3.3) are lower than those of H-SSZ-13(6.0), suggesting that more strongly acidic sites in zeolite are favorable for the formation of alkanes due to enhancement of alkenes hydrogenation.[31,52] This is supported by the catalytic results of H-SAPO-34 with a weaker acid site strength than H-SSZ-13 (Figure S4(b)); the selectivity to propane and that to LPG

are dramatically reduced to 18.8% and 21.3% respectively, while large amounts of $C_2^=$–$C_4^=$ (67.4%) are, as expected, produced (Figures S5(a) and S5(b)). When H-ZSM-35 or H-ZSM-11 is used as zeolite component, a propane selectivity of 17.9% or 38.0% is obtained along with significant amounts of butane and C_5+ alkanes, probably as a result of their larger 10-membered ring (MR) pore openings.

The catalytic performance of $GaZrO_x$(0.5)/H-SSZ-13 for direct conversion of CO_2 into propane is also related to the reaction temperature. At 300 ºC and 3.0 MPa, the selectivity to propane and that to LPG reach 79.8% and 91.8% with a CO_2 conversion of 9.1% and a CO selectivity of just 19.1% (Figures S6(a) and S6(b)). When the reaction temperature is raised to 350 ºC, the CO_2 conversion climbs to 16.3% without seriously influencing propane and LPG selectivities. A further increase in the reaction temperature to 400 ºC elevates the CO_2 conversion to 22.6%, but the selectivity to propane and that to LPG are reduced to 72.9% and 84.0% as more methane (selectivity of 6.2%) and C2 hydrocarbons (selectivity of 7.4% for ethene and ethane) are produced due to the hydrogenolysis of propane at high temperature.[53]

In addition, the reaction pressure has a great effect on the catalytic performance of $GaZrO_x$(0.5)/H-SSZ-13 (Figures S7(a) and S7(b)). At 350 ºC and 0.1 MPa, it shows selectivity to propane and that to LPG of 69.2% and 75.1% respectively, at a CO_2 conversion of 7.7%. An increase in the reaction pressure to 3.0 MPa raises the CO_2 conversion and the selectivities of propane and LPG to 16.3%, 78.9% and 90.4%, respectively, at the serious expense of $C_2^=$–$C_4^=$ selectivity (from 16.5% to < 2.0%), confirming that increase of reaction pressure can effectively promote the alkenes hydrogenation to alkanes.

The effects of gas hourly space velocities (GHSV), the integration manner of $GaZrO_x(0.5)$ oxide and H-SSZ-13 zeolite, and the H_2/CO_2 ratio in feedstock on the catalytic activity and product selectivity of $GaZrO_x(0.5)$/H-SSZ-13 are shown in Figure 2 and Figures S8 and S9. The CO_2 conversion and the selectivity to propane and that to LPG increase with lowering space velocity although more CO emission is generated (Figures S8(a) and S8(b)). At 350 ºC and 3.0 MPa, a decrease of GHSV from 4800 to 1200 mL/(g·h) elevates the CO_2 conversion and the propane and LPG selectivities to 19.0%, 80.4% and 91.2%, respectively. Compared to the granule stacking and the dual bed filling of $GaZrO_x(0.5)$ and H-SSZ-13, the powder mixing of these two components more effectively suppresses the RWGS reaction and hinders the CO production (Figures S9(a) and S9(b)). Increasing the H_2/CO_2 ratio can further enhance the CO_2 conversion and significantly decrease the CO selectivity,[41,42] while it has less effect on the propane and LPG selectivities (Figures 2(a) and 2(b)).

Upon optimization of catalyst preparation method and reaction conditions, the CO_2 conversion is increased to 43.4% with the selectivity to propane and that to LPG maintained at 79.5% and 89.4% (Figures 2c). More interestingly, no considerable increase in the CO selectivity occurs. This results in the propane and LPG yields reaching 23.6% and 26.5% respectively (Figure 2d). To the best of our knowledge, such a high single hydrocarbon product yield has not been achieved yet (Table S1). In addition, an excellent catalytic stability is also observed (Figures 2c and Figures S10). At 350 ºC, 3.0 MPa and H_2/CO_2 ratio of 6/1, the selectivity to propane and that to LPG still get to 74% and 87% respectively along with both the CO_2 conversion and the CO selectivity of around 20% even after reaction of 500 h.

Catalyst characterization. Figure S11(a) shows the x-ray diffraction (XRD) patterns of $GaZrO_x$, and for comparison, of ZrO_2 and Ga_2O_3. Four reflection peaks are observed at 30.5º, 35.5º, 50.6º and 60.2º in the patterns of ZrO_2, which are typically for the (011), (002), (112) and (121) crystal facets of tetragonally structured zirconium oxide (JCPDS NO. 98-0732). These crystal facets are further confirmed by the selected area electron diffraction (SAED) patterns (Figure S12). In addition, the interplanar spacing of 0.294 nm, corresponding to the (011) plane, is observed by the high-resolution transmission electron microscopy (HRTEM) (Figure S13). After incorporation of Ga, the 2θ diffraction peak characteristic of the (011) crystal facet slightly shifts to higher value, and the degree increases with the Ga/Zr ratio from 0 to 1.0 (Figure S11(b)). This is indicative of a shrinkage of unit cell, which is caused by the smaller radius of Ga^{3+} ions (0.40 Å) than that of Zr^{4+} (0.82 Å). The Rietveld refinement results reveal that the unit cell volume gradually declines from 67.24 $Å^3$ to 65.70 $Å^3$ when the Ga/Zr ratio increases from 0 to 1.0 (Table S2). However, for the $GaZrO_x$(4.0), a broad peak is observed in the 2θ range of 30 and 35° (Figure S11(a)). It is similar to that of amorphous Ga_2O_3 (α-Ga_2O_3).[54] The HRTEM images and SAED patterns also confirm no definite crystal structure in $GaZrO_x$(4.0) (Figures S12 and S13). TEM images show that the mean particle size of ZrO_2 is 10.53 nm, and it is decreased to 5.76 nm without change of spherical particle shape after incorporation of proper amounts of Ga ($GaZrO_x$(0.5)) (Figure S14), which significantly enlarges the specific surface area and pore volume (Figure S15 and Table S2). STEM-EDX elemental mapping confirms that Ga, Zr and O elements are uniformly and highly dispersed in the $GaZrO_x$(0.5) sample (Figure S16), indicating that it is a pure solid solution oxide.

The x-ray photoelectron spectra (XPS) of ZrO_2, $GaZrO_x$ and Ga_2O_3 are displayed in Figure S17. The two signals at 184.6 and 182.3 eV in the Zr(3d)-XPS of ZrO_2 are attributed to the $3d_{5/2}$ and $3d_{3/2}$ of Zr (Figure S17(a)),[55] while another two at 1144.7 and 1117.9 eV in the Ga(2p)-XPS of Ga_2O_3 are characteristic of Ga $2p_{3/2}$ and $2p_{1/2}$ (Figure S17(b)).[56] After incorporation of Ga, Zr(3d) signals slightly shift towards lower binding energies, while Ga(2p) shifts to high values. This indicates that Zr and Ga in $GaZrO_x$ oxide have strong interaction, supporting the incorporation of Ga in ZrO_2 lattice sites and formation of $GaZrO_x$ solid solution.[33] Figure S18 shows that four types of oxygen species, viz. lattice oxygen species ($O_{lattice}$, 529.5 eV), O atoms around defect sites (O_{defect}, 530.5 eV), O atoms in surface hydroxyl groups (–OH, 531.8 eV), and O atoms of surface-adsorbed molecular water (H_2O, 532.5 eV) are present in all the prepared oxides.[57] A comparison of the peak intensity around 530.5 eV shows that $GaZrO_x$(0.5) and $GaZrO_x$(4.0) contain more surface oxygen vacancies than ZrO_2 and Ga_2O_3, thus promoting the adsorption of CO_2. This is supported by the CO_2-TPD results. The two peaks at high temperature (150–320 °C (β peak) and 320–600 °C (γ peak)) intensify with the incorporated Ga amount (Figure S19). These two peaks are due to desorption of CO_2 moderately and strongly chemisorbed on the surface oxygen vacancies respectively.[58,59] It further substantiates that incorporation of Ga in ZrO_2 generates more oxygen vacancies on the surface. The density functional theory (DFT) computation results reveal that $GaZrO_x$ exhibits a lower energy for the formation of surface oxygen vacancies than ZrO_2 (Figure S20).

Figure S19 shows that larger amounts of CO_2 are desorbed from $GaZrO_x$(4.0) than from $GaZrO_x$(0.5) between 320 – 600 °C, indicative of presence of more surface oxygen

vacancies in $GaZrO_x$(4.0). This is in line with the DFT calculation result that $GaZrO_x$(4.0) shows higher CO_2 adsorption energy than $GaZrO_x$(0.5) and ZrO_2 (Figure S21), which originates from its stronger electronic interaction with CO_2 molecule, as confirmed by projected density of states (PDOS) (Figure S22) and charge difference density (CDD) results (Figure S23). However, highly strong CO_2 adsorption prevents its desorption and may even lead to C-O bond breaking of CO_2 to form CO,[60,61] and hence, unfavorably forming methanol. Indeed, the methanol STY of $GaZrO_x$(4.0) is decreased, whereas it produces more CO than $GaZrO_x$(0.5) (Figure S3). This suggests that the moderately adsorbed CO_2 on the surface oxygen vacancies of $GaZrO_x$(0.5) should be mostly transformed into methanol.

Figure S24 and Table S3 show that all the H-SSZ-13 zeolites synthesized with synthesis gels with Si/Al ratios in the range of 6.0 – 22.0 are pure CHA phase having high crystallinity, large specific surface areas and similar pore volumes. The SEM images reveal that these H-SSZ-13 zeolites possess an ellipsoid-like habit with a particle size around 0.5 – 1 μm (Figure S25). The ^{27}Al MAS NMR spectroscopy evidences that most of Al atoms are incorporated in the framework, as a sharp resonance peak was observed between 45 and 65 ppm with a very small peak at 0 − 10 ppm (Figure S26). However, when the Si/Al ratio in H-SSZ-13 is decreased to 3.3, the crystallinity, specific surface area and pore volume are heavily decreased (Figure S24 and Table S3), which is consistent with the ^{27}Al MAS NMR spectral result; more octahedral extra-framework Al species are present in H-SSZ-13(3.3) (Figure S26).

The NH_3-TPD profiles of H-SSZ-13 zeolites are characterized by two peaks centered at 150−200 ºC and 400−600 ºC, which are caused by desorption of NH_3 molecules interacted

with weak and strong acid sites, respectively (Figure S4(a)). Except for the H-SSZ-13(3.3), increase of the Si/Al ratio decreases the total acid site content (Table S3), but the number and strength of strong acid sites exhibit a volcanic function. H-SSZ-13(9.6), followed by H-SSZ-13(6.0), possesses more strong acid sites, also with higher acid strength (Figure S4(a) and Table S3). This is supported by the NH_3-IR results (Figure S27); more than 70% and about 62% of acid sites in H-SSZ-13(9.6) and H-SSZ-13(6.0) are strong Brøsted acid sites in contrast to ≤ 57% for H-SSZ-13(3.3), H-SSZ-13(15.6) and H-SSZ-13(22.0). This suggests that higher yields of propane and LPG obtained on the $GaZrO_x$(0.5)/H-SSZ-13(6.0) and $GaZrO_x$(0.5)/H-SSZ-13(9.6) should be related to their larger numbers of strong Brønsted acid sites with higher acid strength, which enhances the alkene hydrogenation to alkane. This is substantiated by the catalytic results of $GaZrO_x$(0.5)/H-SAPO-34; the selectivity to propane and that to LPG are significantly lower as a result of generation of more $C_2^=$–$C_4^=$. H-SAPO-34 has the same CHA topological structure and exhibits comparable total acid sites amount, specific surface area and pore volume as H-SSZ-13(6.0) (Figure S28 and Table S3), but possesses smaller numbers of strong acid sites with lower acid strength (Figure S4(b) and Figure S28(d)).

Reaction mechanism. The detailed reaction mechanism for conversion of CO_2 into propane was investigated by combining isotope-labeled in situ DRIFTS, ^{13}C MAS NMR with pulse-quenched method, GC-MS, various probe experiments and DFT calculations. Figure 3 and Figures S29 and S30 show the in situ DRIFT spectra of ZrO_2, $GaZrO_x$(0.1), $GaZrO_x$(0.5) and $GaZrO_x$(4.0) oxides for hydrogenation of CO_2 to methanol. For the $GaZrO_x$(0.5) oxide, the peaks between 1450 and 1500 cm^{-1} are attributed to monodentate and/or bidentate

carbonate species that are formed by chemical adsorption of CO_2 on surface oxygen vacancies.[62,63] After reaction of 1 min, the peaks at 1585, 1386 and 1373 cm^{-1}, corresponding to the C=O stretching and C-H bending vibrations of surface formate species,[64,65] appear and increase in the intensity with the reaction time (Figure 3(a1)). When the reaction was carried out for 5 min, another two peaks assigned to the C−O stretching vibrations and the CH_3 bending vibrations of methoxy species are detected at about 1143 and 1060 cm^{-1} (Figure 3(a2)).[38,66] In addition, the peaks for the C−H asymmetric and symmetric stretching vibrations of formate and methoxy species are clearly visible at 2885 and 2969 cm^{-1}, and 2825 and 2930 cm^{-1}, respectively (Figure 3(a3)).[38,64–66] These results demonstrate that the CO_2 molecules adsorbed on the $GaZrO_x(0.5)$ surface oxygen vacancies can rapidly react with active H* to form formate and methoxy intermediates, which are further hydrogenated into methanol.

The above-mentioned peaks could be observed in the DRIFTS of ZrO_2, $GaZrO_x(0.1)$ and $GaZrO_x(4.0)$ too, but the intensities of these peaks are largely different (Figures 3(b1–b3) and Figures S29 and S30). The intensity of peaks characteristic of formate and methoxy species decreases in the order of $GaZrO_x(0.5)$ > $GaZrO_x(4.0)$ > $GaZrO_x(0.1)$ > ZrO_2 (Figure S31). It is further confirmed by isotope-labeled in situ DRIFT spectroscopy. When CO_2 and D_2 were fed on the catalyst at 300 ºC for 2 min, a broad band was observed between 2160 and 2190 cm^{-1} (Figure 4(a–c)), which is assigned to the C-D vibration of deuterium-labeled formate species (DCOO*).[33] This broad band quickly enhanced with the reaction time, and $GaZrO_x(0.5)$ shows higher intensity than ZrO_2 and $GaZrO_x(4.0)$. Such a phenomenon was also observed for the C-D vibration band of deuterium-labeled methoxy species (CD_3O*) at

about 2060 cm^{-1},[11] although it became visible after reaction of 10 min. The ^{13}C MAS NMR spectra for converting $^{13}CO_2$ and H_2 at 300 ºC show a sharp band attributed to the ^{13}C-labeled formate ($H^{13}COO^*$) species[41] at 170 ppm (Figure 4(d)), and it is more intense for $GaZrO_x(0.5)$ than for ZrO_2 and $GaZrO_x(4.0)$. These spectroscopy results indicate that incorporation of Ga into ZrO_2 enhances the adsorption and activation of CO_2 molecules, thus resulting in the formation of more formate and methoxy intermediates, although addition of too much Ga, e.g. for the $GaZrO_x(4.0)$ sample, gives a contrary result due to over-strong adsorption of CO_2 on the surface oxygen vacancies (Figures S19, S22 and S23).

The formed methanol on $GaZrO_x$ oxides is then transformed into hydrocarbons on the Brønsted acid sites in H-SSZ-13 via the hydrocarbon pool (HCP) mechanism.[67] Figure 5(a) shows that the amount of aromatic HCP species, such as polymethylbenzenes (polyMBs) and polymethylnaphthenes (polyMNs), clearly decreases with increasing Si/Al ratio of H-SSZ-13 from 3.3 to 9.6, while substantially rises when the Si/Al ratio is further increased to 15.6 and 22.0. This is unexpected as the acid strength and content of strong acid sites of H-SSZ-13 exhibit a volcanic relationship with its Si/Al ratio (Figure S4(a), Figure S27 and Table S3). It seems that the presence of large numbers of highly acidic strong acid sites in H-SSZ-13 is unfavorable for formation of aromatic species. This is supported by the catalytic results of H-SAPO-34 zeolite with smaller numbers of strong acid sites with weaker acid strength (Figure S4(b), Figure S28(d) and Table S3); it produces far more aromatic species than H-SSZ-13 at the same reaction conditions (Figure 5(b)). The TG analysis results further substantiate this point. $GaZrO_x(0.5)$/H-SSZ-13(6.0) and $GaZrO_x(0.5)$/H-SSZ-13(9.6) show a much lower coking rate than H-SAPO-34 and other H-SSZ-13 samples (Figure 5(d) and

Figure 5(e)). This indicates that at high H_2 pressure, increase of strong acid site amount and strength of H-SSZ-13 significantly suppresses the formation of aromatic HCP species,[68] thus weakening the aromatics-based cycle, but relatively enhancing the alkene-based cycle.[69,70] This leads to production of fewer amounts of C2 hydrocarbons (ethene and ethane) but more propene and butene that are quickly hydrogenated to propane and butane on strong acid sites. This is supported by the finding that the propane amount linearly increases with the content of strong acid sites in H-SSZ-13 (including H-SAPO-34) zeolite (Figure 5(c)). It is consolidated by the result obtained with $GaZrO_x$(0.5) substituted by other typical oxides such as $ZnZrO_x$(0.5) and $InZrO_x$(0.5); propane is still the dominant product with selectivity >75% (Figures S32 and S33).

Figure S34(a) shows the catalytic results for conversion of methanol on H-SSZ-13 and H-SAPO-34 zeolites. Clearly, propane (selectivity of 72.7%) and butane (selectivity of 10.8%) are the main products at the initial reaction stage on H-SSZ-13(6.0) in H_2 atmosphere, as observed by Davis and co-workers.[71] However, the propane selectivity quickly decreases along with formation of considerable amounts of light olefins with the reaction time. This is probably due to rapid coking that leads to serious coverage of strong acid sites, which facilitates formation of aromatic HCP species by weakening their hydrogenolysis, and thus, typical MTO product distribution was obtained.[72,73] This is proved by attaining high propane selectivity (> 60%) within longer reaction time when decreasing methanol weight hourly space velocity (WHSV) from 2.0 to 0.24 h^{-1} (Figure S34(a-c) and Figure 6(a2)). Another piece of evidence is observing of a more evident decline of propane selectivity when the carrier gas is changed from H_2 to Ar (Figure 6(a1) and Figure 6(a2)).

Figure 6 reveals that the H_2 pressure has a strong effect on the propane selectivity and catalytic life. At 350 ºC, 3.0 MPa and $WHSV_{methanol}$ of 0.24 h^{-1}, the propane selectivity can be maintained at 56% over H-SSZ-13 after reaction of 14 h (Figure 6(a3)). However, lowering of the H_2 pressure to 0.1 MPa quickly decreases the propane selectivity below 50% within 5.5 h (Figure 6(a2)). Figure S35 shows that high H_2 pressure suppresses formation of aromatic HCP species,[72,73] consequently, promoting production of more C3 (propane+propene) and C4 species (butane+butene) but smaller amounts of C2 (ethene+ethane) (Figure S36). Thus, it can be concluded that high propane selectivity of $GaZrO_x$(0.5)/H-SSZ-13 in CO_2 hydrogenation is due to attenuation of the aromatics-based cycle.

As expected, H-SAPO-34 shows typical MTO product distribution with $C_2^=$–$C_4^=$ selectivity of 87.9% in Ar atmosphere (Figure 6(b1)). Although a change of the carrier gas from Ar to H_2 increases the initial propane selectivity from 8.9% to 26.3% (Figure 6(b2)), it is far lower than that obtained on H-SSZ-13(6.0) (propane selectivity of 83.9%) at the same reaction conditions (Figure 6(a2)). Moreover, the propane selectivity quickly decreased below 10% with increasing reaction time to 5.5 h, while more C2 hydrocarbons (mainly ethene (23.3%)) are produced (Figure 6(b2)). Despite that increase of H_2 reaction pressure to 3.0 MPa can elevate the propane selectivity to 59.8% at 0.5 h, it rapidly declined to 3.5% at 8 h (Figure 6(b3)). In contrast, high propane selectivity (around 56%) is obtained on H-SSZ-13(6.0) at least within 14 h (Figure 6(a3)). The much lower propane selectivity of H-SAPO-34 results from its weaker Brønsted acidity (Figure S4(b), Figure S28(d) and Table S3), which enhances the aromatics-based cycle, and consequently, produces more C2

hydrocarbons (ethene and ethane) (Figures 6(b1)-5(b3)).

The intrinsic kinetics of various elemental reactions in MTO process over H-SSZ-13 and H-SAPO-34 are investigated by DFT calculations. The 1-hexene can be generated by repeatedly methylating initial light olefins ($C_2^=$ – $C_4^=$) with free energy barrier of 122–136 kJ mol^{-1} (Figure 7 and Figure S37). It is more possibly produced through $C_2^=$ – $C_4^=$ oligomerizations as their free energy barriers are slightly lower (112–125 kJ mol^{-1}). Regardless of the carbon chain growth pathway, the β-scission of 1-hexene to propene is energetically more favorable than the cracking to ethene and butene due to lower free energy barrier (98 vs. 113 kJ mol^{-1}). Further methylation of 1-hexene to 1-heptene suffers from serious space confinement, causing the free energy barrier rise to 141 kJ mol^{-1}. Even if this reaction occurs, the formed 1-heptene would be primarily cracked into one propene and one butene via β-scission mechanism (107 kJ mol^{-1}) rather than one ethene and one pentene (116 kJ mol^{-1}). Figure 7 shows that the formed propene and butene are hydrogenated into corresponding alkanes, not cyclized and subsequently dehydrogenated into aromatics through hydride transfer reactions, as the former reactions (123 and 120 kJ mol^{-1}) require lower free energy barriers than the latter (150 kJ mol^{-1}). In addition, it needs to point out that the generated aromatic species in H-SSZ-13 zeolite are highly unstable in the H_2 atmosphere. This is because the hydrogenolysis reaction between the aromatics and H_2 just surpasses a free energy barrier of 43 – 112 kJ mol^{-1}. It is substantiated by seriously decreasing coking rate in methanol conversion upon change of the carrier gas from Ar to H_2 and increasing H_2 pressure (Figure S38). The effect of generated CO through RWGS on the coking rate in methanol conversion can be excluded as no obvious difference was observed with Ar and

with 10%CO/Ar as carrier gas (Figure S39). The above calculation results indicate that propene as dominant product is generated from the alkene-based cycle, but it is rapidly hydrogenated to propane on the strong acid sites of H-SSZ-13. This is consolidated by the results for conversion of 1-hexene on H-SSZ-13 at 350 ºC and 1.5 MPa in H_2 atmosphere; the selectivity to propane reaches 75%, while that to light olefins is < 0.1%, along with detection of few amounts of aromatic species by GC-MS in used H-SSZ-13 (Figures S40(a) and S41).

Similarly, 1-hexene is also formed via both successive methylations and oligomerization of $C_2^=$ – $C_4^=$, and also inclined to cracking into propene rather than ethene and butene on H-SAPO-34 (108 vs. 130 kJ mol^{-1}, Figure S37). Notably, although its aromatization following cyclization and hydride transfer reaction crosses slightly higher free energy barrier (160 kJ mol^{-1} and 120 – 125 kJ mol^{-1}) than that on H-SSZ-13, the generated aromatic species is rather stable on H-SAPO-34 even in H_2 atmosphere, as its hydrogenolysis demands 180 kJ mol^{-1} in terms of the rate-determining step (Figure S37). Thus, once the aromatic species are formed, it will be accumulated in H-SAPO-34 and rapidly propagated, as confirmed by detecting larger amounts of bulky aromatic residues in used H-SAPO-34 (Figure S41). Another piece of evidence is that changing carrier gas from Ar to H_2 or increasing the pressure of H_2 has insignificant influence on the coking rate (Figure S42). Moreover, it is found that hydrogenation of generated propene to propane requires more demanding free energy barrier on H-SAPO-34 (160 kJ mol^{-1}) than on H-SSZ-13 (123 kJ mol^{-1}). Consequently, conversion of 1-hexene on H-SAPO-34 gave propane selectivity as low as 39.8%, but light olefins selectivity of 22.5% (Figure S40(b)).

Discussion

A new catalyst system consisting of $GaZrO_x$ oxide and H-SSZ-13 zeolite has been prepared, and it shows excellent catalytic performance for direct hydrogenation of CO_2 into propane. The selectivity of propane and LPG (propane+butane) can reach 79.5% and 89.4%, at CO_2 conversion of 43.4%, but undesired CO selectivity is only 31.8% at 350 ºC and 3.0 MPa. This results in the propane and the LPG yields as high as 23.6% and 26.5%, respectively. This extraordinary catalytic performance is well maintained as least 500 h. The results of isotope-labeled in situ DRIFTS, ^{13}C MAS NMR with pulse-quenched method, GC-MS, various probe experiments and DFT calculations demonstrate that the high concentration of surface oxygen vacancies and the moderate adsorption strength of CO_2 molecules on $GaZrO_x(0.5)$ enhance methanol production by forming more formate and methoxy intermediates. Subsequently, the generated methanol quickly diffuses onto zeolites and transforms into hydrocarbons via the HCP mechanism. At high H_2 pressure, stronger Brøsted acid sites of H-SSZ-13 zeolite can effectively inhibit the formation of aromatic HCP species, thus significantly decreasing the contribution of aromatic-based cycle, but enhancing the alkene-based cycle. As a result, the formation of C2 hydrocarbons (ethene and ethane) is suppressed, while that of propene and butene is promoted. The produced olefins are quickly hydrogenated to corresponding alkanes on the strong acid sites of H-SSZ-13 (Figure 8). This work provides not only a highly efficient catalyst system for selective conversion of CO_2 into propane but also new insights into precisely controlling the catalytic reaction pathways and finely tuning the product distribution in CO_2 hydrogenation.

Method

Catalyst preparation. Zirconium oxide (ZrO_2), gallium oxide (Ga_2O_3) and gallium-zirconium oxides ($GaZrO_x$(N), N represents the Ga/Zr molar ratio) were prepared by the sol-gel method. First, designed amounts of zirconium nitrate ($Zr(NO_3)_4$) or gallium nitrate ($Ga(NO_3)_3$), and/or zirconium nitrate ($Zr(NO_3)_4$) and gallium nitrate ($Ga(NO_3)_3$) mixture with the Ga/Zr molar ratio of 0.1, 0.25, 0.5, 1.0, 2.0 and 4.0 were dissolved in deionized water (150 mL) and stirred at room temperature for 2 h. Then, the glucose was slowly added at 80 °C and vigorously stirred for at least 8 h. The molar ratio of glucose to the total metal ions in the solution is 3.0. The obtained colloid was dried at 100 °C for 12 h, and sequentially calcined at 300 and 500 °C for 1 and 3 h respectively in air.

SSZ-13 (CHA), SAPO-34 (CHA), ZSM-11 (MEL) and ZSM-35 (FER) zeolites were prepared by the hydrothermal synthesis method. SSZ-13 zeolite was synthesized with aluminum sulfate ($Al_2(SO_4)_3$), silica sol (JN-25), N,N,N-trimethyl-1-adamantam monium hydroxide (TMAdaOH), deionized water and potassium hydroxide (KOH) with the chemical compositions of $1.0SiO_2$: xAl_2O_3: 0.4TMAdaOH: 0.6KOH: $88H_2O$ (x = 0.151, 0.083, 0.052, 0.032 and 0.023). The mixture was stirred at room temperature for 3 h. For SAPO-34 zeolite, the silica sol (JN-40), phosphoric acid (H_3PO_4), pseudo-boehmite (Al_2O_3), tetraethyl ammonium hydroxide (TEAOH) and deionized water were mixed and stirred at room temperature for 2 h in terms of a composition of 2.0TEAOH: $0.3SiO_2$: $1.0Al_2O_3$: $1.0P_2O_5$: $70H_2O$. ZSM-11 zeolite was prepared by using the silica sol (JN-40), deionized water, tetrabutylammonium hydroxide (TBAOH), sodium aluminate ($NaAlO_2$) and sodium hydroxide (NaOH) with the ratio of mixture of 12TBAOH: $5.0Al_2O_3$: $120SiO_2$: $1420H_2O$:

8.6Na_2O. The obtained mixture was then stirred at room temperature for 2 h. ZSM-35 zeolite was synthesis with the silica sol (JN-40), pyrrolidine (PYR), sodium hydroxide (NaOH), sodium aluminate ($NaAlO_2$) and deionized water. The mixture was stirred at room temperature for 4 h. The obtained gel had a composition of 1.85Na_2O: 1.0Al_2O_3: 20SiO_2: 19.7PYR: 592H_2O.

The resultant gel was then transferred into a Teflon-lined stainless-steel autoclave and crystallized at 150 °C for 144 h for SSZ-13, 200 °C for 20 h for SAPO-34, 170 °C for 20 h and 48 h for ZSM-11 and ZSM-35, respectively. Various H-type zeolite samples of H-SSZ-13, H-ZSM-11 and H-ZSM-35 were obtained by repeatedly ion-exchanging calcined Na-type samples with 1 M NH_4NO_3 aqueous solution at 80 °C for three times, drying at 100 °C for 12 h, and calcining at 560 °C for 5 h. For the preparation of H-SAPO-34, the as-synthesized sample was directly calcined at 550 °C for 10 h in air.

Catalyst characterization. The prepared catalysts were characterized by the X-ray diffraction (XRD), N_2 sorption, X-ray photoelectron spectra (XPS), transmission electron microscopy (TEM), high-resolution TEM (HRTEM), scanning transmission electron microscopy (STEM) and energy-dispersive x-ray spectroscopy (EDX) elemental mapping, scanning electron microscopy (SEM), temperature programmed desorption of CO_2 or NH_3 (CO_2-TPD or NH_3-TPD), ammonia-adsorbed Fourier transform infrared spectroscopy (NH_3-IR), ^{13}C and ^{27}Al magic angle spinning nuclear magnetic resonance (^{13}C/^{27}Al MAS NMR), thermogravmetric (TG) analysis, in situ diffuse reflectance infrared Fourier transform spectra (DRIFTS) and gas chromatography−mass spectrometry (GC-MS) spectroscopy. More information about the characterization methods could be seen in Supplementary Information.

DFT calculation. Periodic density functional theory (DFT) calculations within the generalized gradient approximation (GGA) were conducted with the Vienna *ab initio* Simulation Package (VASP 5.3.5). The Perdew, Burke, and Ernzrhof (PBE) exchange-correlation functional was applied, and the projected augmented wave (PAW) method was employed to represent the electron−ion interactions. More information about the DFT calculation methods could be seen in Supplementary Information.

Catalytic evaluation. CO_2 conversion was carried out in a stainless steel tubular fixed-bed reactor with an inner diameter of 10 mm. 1.0 g Composite catalyst (20−40 mesh) prepared by mixed the power of the ZrO_2, Ga_2O_3 or $GaZrO_x$(N) oxide and H-SSZ-13 zeolite with mass ratio of 1/2 was loaded unless being specifically stated. Before the reaction, the catalyst was pre-reduced at 400 ºC and atmospheric pressure for 2 h in a pure H_2 flow (30 mL/min). Then, it was cooled to 350 ºC in a N_2 flow (30 mL/min). The CO_2 and H_2 with a CO_2/H_2 of 1/3 (with 3 vol.% N_2 as internal standard) was introduced in the reactor at 350 ºC, 3.0 MPa and 2400 mL/(g·h) unless otherwise stated. The effluent products were online analyzed using an Agilent 7890A gas chromatograph (GC) equipped with one TCD and two flame ionization detectors (FID) and two capillary columns (J&W 127-7031, 30 m × 530 μm × 0.25μm; Agilent 19095P-S25, 50 m × 530 μm × 15 μm). The product selectivity (not include CO) was calculated on a molar carbon basis. The CO_2 conversion was calculated by the equation (1), and the selectivity to hydrocarbons (including alkenes and alkanes, C_nH_m) and oxygenates (including methanol (CH_3OH) and dimethyl ether (DME)) were calculated by the equations (3) and (4), respectively, without considering CO. The CO emission was separately evaluated by the equation (2), as reported by other researchers.[36–40] The carbon

molar balances were at least 95%.

$$CO_2 \text{ conversion} = \frac{CO_{2in} - CO_{2out}}{CO_{2in}} \times 100\% \quad (1)$$

$$CO \text{ selectivity} = \frac{CO_{out}}{CO_{2in} - CO_{2out}} \times 100\% \quad (2)$$

where CO_{2in} and CO_{2out} are the inlet and outlet amounts (moles) of CO_2 respectively; CO_{out} is the outlet amount (mole) of CO.

C_nH_m selectivity = $n_{CnHm}/\sum(C_nH_m + \text{oxygenates}) \times 100\%$; (3)

Oxygenates selectivity = $n_{oxygenates}/\sum(C_nH_m + \text{oxygenates}) \times 100\%$; (4)

where n_{CnHm} is the amount (carbon moles) of individual hydrocarbon product at the outlet and $\sum(C_nH_m + \text{oxygenates})$ is the total carbon mole of products, including hydrocarbons and oxygenates. The catalytic results obtained at reaction time of 28 h were generally used for comparison.

The methanol conversion and hexene conversion were performed in the same fixed-bed reactor. The zeolite catalyst (20−40 mesh) was first pretreated at 400 ºC and atmospheric pressure for 2 h. Then, the reaction was conducted at 350 ºC and different reaction pressures. Methanol or hexene was continuously introduced into the reactor by an infusion pump with a weight hourly space velocity (WHSV) of 2.0, 1.0, 0.5 or 0.24 h^{-1} under the Ar or H_2 (30 mL min^{-1}) atmosphere. The effluent products were online analyzed using a same Agilent 7890A gas chromatograph (GC) in the CO_2 conversion reaction. The methanol conversion ($x_{methanol}$) or hexene conversion (x_{hexene}) and the selectivity to product i (s_i) were calculated by the following equations:

$$x_{\text{methanol}} = \left(n_{\text{methanol,in}} - n_{\text{methanol,out}}\right)/n_{\text{methanol,in}} \times 100\%$$

$$x_{\text{hexene}} = \left(n_{\text{hexene,in}} - n_{\text{hexene,out}}\right)/n_{\text{hexene,in}} \times 100\%$$

$$s_i = n_i \cdot k_i / \sum n_i \cdot k_i \times 100\%$$

where n_i is the molar quantity of product i in the effluents and k_i is the number of carbon atoms in its molecule.

Data Availability. The data that support the findings of this study including the article and its Supplementary Information are available from the corresponding authors upon a reasonable request.

References

(1) Centi, G., Quadrelli, E. A. & Perathoner, S. Catalysis for CO_2 conversion: a key technology for rapid introduction of renewable energy in the value chain of chemical industries. *Energy Environ. Sci*. **6**, 1711–1731 (2013).

(2) Bushuyev, O. S., de Luna, P., Dinh, C. T., Tao, L., Saur, G., van de Lagemaat, J., Kelley, S. O. & Sargent, E. H. What should we make with CO_2 and how can we make it? *Joule* **2**, 825–832 (2018).

(3) Porosoff, M. D. Yan, B. & Chen, J. G. Catalytic reduction of CO_2 by H_2 for synthesis of CO, methanol and hydrocarbons: challenges and opportunities. *Energy Environ. Sci*. **9**, 62–73 (2016).

(4) Liu, Y. T., Deng D. H. & Bao, X. H. Catalysis for selected C1 chemistry. *Chem* **6**, 2497–2514 (2020).

(5) Alvarez, A., Bansode, A., Urakawa, A., Bavykina, A. V., Wezendonk, T. A., Makkee, M., Gascon, J. & Kapteijn, F. Challenges in the greener production of formates/formic acid, methanol, and DME by heterogeneously catalyzed CO_2 hydrogenation processes. *Chem. Rev*. **117**, 9804−9838 (2017).

(6) Wang, W., Wang, S., Ma, X. & Gong, J. Recent advances in catalytic hydrogenation of carbon dioxide. *Chem. Soc. Rev*. **40**, 3703–3727 (2011).

(7) Zhong, J. W., Yang, X. F., Wu, Z. L., Liang, B. L., Huang, Y. Q. & Zhang, T. State of the art and perspectives in heterogeneous catalysis of CO_2 hydrogenation to methanol. *Chem. Soc. Rev*. **49**, 1385–1413 (2020).

(8) Bao, J., Yang, G. H., Yoneyama, Y. & Tsubaki, N. Significant advances in C1 catalysis: highly efficient catalysts and catalytic reactions. *ACS Catal*. **9**, 3026−3053 (2019).

(9) Ye, R. P., Ding, J., Gong, W. B., Argyle, M. D., Zhong, Q., Wang, Y. J., Russell, C. K., Xu, Z. H., Russell, A. G., Li, Q. H., Fan, M. H. & Yao, Y. G. CO_2 hydrogenation to high-value products via heterogeneous catalysis. *Nat. Commun*. **10**, 5698 (2019).

(10) Studt, F., Sharafutdinov, I., Abild-Pedersen, F., Elkjaer, C. F., Hummelshoj, J. S., Dahl, S., Chorkendorff, I. & Norskov, J. K. Discovery of a Ni-Ga catalyst for carbon dioxide reduction to methanol. *Nat. Chem*. **6**, 320−324 (2014).

(11) Wu, C. Y., Lin, L. L., Liu, J. J., Zhang, J. P., Zhang, F., Zhou, T., Rui, N., Yao, S. Y., Deng, Y. C., Yang, F., Xu, W. Q., Luo, J., Zhao, Y., Yan, B. H., Wen, X. D., Rodirguez, J. A. & Ma, D. Inverse ZrO_2/Cu as a highly efficient methanol synthesis catalyst from CO_2 hydrogenation. *Nat. Commun*. **11**, 5767 (2020).

(12) Zhu, Y. F., Zheng, J., Ye, J. Y., Cui, Y. R., Koh, K., Kovarik, L., Camaioni, D. M.,

Fulton, J. L., Truhlar, D. G., Neurock, M., Cramer, C. J., Gutierrez, O. Y. & Lercher, J. A. Copper-zirconia interfaces in UiO-66 enable selective catalytic hydrogenation of CO_2 to methanol. *Nat. Commun*. **11**, 5849 (2020).

(13) Wang, L. X., Guan, E. J., Wang, Y. Q., Wang, L., Gong, Z. M., Cui, Y., Meng, X. J., Gates, B. C. & Xiao, F. S. Silica accelerates the selective hydrogenation of CO_2 to methanol on cobalt catalysts. *Nat. Commun*. **11**, 1033 (2020).

(14) He, M. Y., Sun Y. H. & Han, B. X. Green carbon science: Scientific basis for integrating carbon resource processing, utilization, and recycling. *Angew. Chem., Int. Ed*. **52**, 9620–9633 (2013).

(15) von der Assen, N., Voll, P., Peters M. & Bardow, A. Life cycle assessment of CO_2 capture and utilization: a tutorial review. *Chem. Soc. Rev*. **43**, 7982–7994 (2014).

(16) Gutterod, E. S., Lazzarini, A., Fjermestad, T., Kaur, G., Manzoli, M., Bordiga, S., Svelle, S., Lillerud, K. P., Skulason, E., Oien-Odegaard, S., Nova, A. & Olsbye, U. Hydrogenation of CO_2 to methanol by Pt nanoparticles encapsulated in UiO-67: Deciphering the role of the metal−organic framework. *J. Am. Chem. Soc*. **142**, 999−1009 (2020).

(17) Frei, M. S., Mondelli, C., Cesarini, A., Krumeich, F., Hauert, R., Stewart, J. A., Ferre, D. C. & Perez-Ramirez, J. Role of zirconia in indium oxide-catalyzed CO_2 hydrogenation to methanol. *ACS Catal*. **10**, 1133−1145 (2020).

(18) Jiang, X., Nie, X. W., Guo, X. W., Song, C. S. & Chen, J. G. G. Recent advances in carbon dioxide hydrogenation to methanol via heterogeneous catalysis. *Chem. Rev*. **120**, 7984−8034 (2020).

(19) Xie, S. J., Ma, W. C., Wu, X. J., Zhang, H. K., Zhang, Q. H. Wang, Y. D. & Wang, Y. Photocatalytic and electrocatalytic transformations of C1 molecules involving C–C coupling. *Energy Environ. Sci*. **14**, 37−89 (2021).

(20) Torres Galvis, H. M., Bitter, J. H., Khare, C. B., Ruitenbeek, M., Dugulan, A. I. & de Jong, K. P. Supported iron nanoparticles as catalysts for sustainable production of lower olefins. *Science* 335, 835–838 (2012).

(21) Wei, J., Ge, Q. J., Yao, R. W., Wen, Z. Y., Fang, C. Y., Guo, L. S., Xu, H. Y. & Sun, J. Directly converting CO_2 into a gasoline fuel. *Nat. Commun*. **8**, 16170 (2017).

(22) Ramirez, A., Dutta Chowdhury, A., Dokania, A., Cnudde, P., Caglayan, M., Yarulina, I., Abou-Hamad, E., Gevers, L., Ould-Chikh, S., De Wispelaere, K., Van Speybroeck, V. & Gascon, J. Effect of zeolite topology and reactor configuration on the direct conversion of CO_2 to light olefins and aromatics. *ACS Catal*. **9**, 6320−6334 (2019).

(23) Xu, Y. Zhai, P., Deng, Y. C., Xie, J. L., Liu, X., Wang, S. & Ma, D. Highly selective olefin production from CO_2 hydrogenation on iron catalysts: A subtle synergy between manganese and sodium additives. *Angew. Chem. Int. Ed*. **59**, 21736–21744 (2020).

(24) Wang, C. T., Guan, E. J., Wang, L., Chu, Y. F., Wu, Z. Y., Zhang, J., Yang, Z. Y., Jiang, Y. W., Zhang, L., Meng, X. J., Gates, B. C. & Xiao, F. S. Product selectivity controlled by nanoporous environments in zeolite crystals enveloping rhodium nanoparticle catalysts for CO_2 hydrogenation. *J. Am. Chem. Soc*. **141**, 8482−8488 (2019).

(25) Paalanen, P. P., Van Vreeswijk, S. H. & Weckhuysen, B. M. Combined In situ x-ray powder diffractometry/raman spectroscopy of iron carbide and carbon species evolution in Fe(-Na-S)/α-Al_2O_3 catalysts during Fischer-Tropsch synthesis. *ACS Catal*.

10, 9837−9855 (2020).

(26) Zhang, Z. P., Zhang, J., Wang, X., Si, R., Xu, J. & Han, Y. F. Promotional effects of multiwalled carbon nanotubes on iron catalysts for Fischer-Tropsch to olefins. *J. Catal*. **365**, 71–85 (2018).

(27) Li, J., He, Y. L., Tan, L., Zhang, P. P., Peng, X. B., Oruganti, A., Yang, G. H., Abe, H., Wang, Y. & Tsubaki, N. Integrated tuneable synthesis of liquid fuels via Fischer–Tropsch technology. *Nat. Catal*. 1, 787–793 (2018).

(28) Torres Galvis, H. M. & de Jong, K. P. Catalysts for production of lower olefins from synthesis gas: a review. *ACS Catal*. **3**, 2130–2149 (2013).

(29) Zhou, W., Cheng, K., Kang, J. C., Zhou, C., Subramanian, V., Zhang, Q. H. & Wang, Y. New horizon in C1 chemistry: breaking the selectivity limitation in transformation of syngas and hydrogenation of CO_2 into hydrocarbon chemicals and fuels. *Chem. Soc. Rev*. **48**, 3193−3228 (2019).

(30) Jiao, F., Li, J. J., Pan, X. L., Xiao, J. P., Li, H. B., Ma, H., Wei, M. M., Pan, Y., Zhou, Z. Y., Li, M. R., Miao, S., Li, J., Zhu, Y. F., Xiao, D., He, T., Yang, J. H., Qi, F., Fu, Q. & Bao, X. H. Selective conversion of syngas to light olefins. *Science* **351**, 1065–1068 (2016).

(31) Cheng, K., Gu, B., Liu, X. L., Kang, J. C., Zhang, Q. H. & Wang, Y. Direct and highly selective conversion of synthesis gas to lower olefins: design of a bifunctional catalyst combining methanol synthesis and carbon-carbon coupling. *Angew. Chem. Int. Ed*. **55**, 4725–4728 (2016).

(32) Dang, S. S., Qin, B., Yang, Y., Wang, H., Cai, J., Han, Y., Li, S. G., Gao, P. & Sun, Y.

H. Rationally designed indium oxide catalysts for CO_2 hydrogenation to methanol with high activity and selectivity. *Sci. Adv*. **6**, eaaz2060 (2020).

(33) Wang, J. J., Li, G. N., Li, Z. L., Tang, C. Z., Feng, Z. C., An, H. Y., Liu, H. L., Liu, T. F. & Li, C. A highly selective and stable ZnO-ZrO_2 solid solution catalyst for CO_2 hydrogenation to methanol. *Sci. Adv*. **3**, e1701290 (2017).

(34) Jiao, F., Pan, X. L., Gong, K., Chen, Y. X., Li, G. & Bao, X. H. Shape-selective zeolites promote ethylene formation from syngas via a ketene intermediate. *Angew. Chem. Int. Ed*. **57**, 4692–4696 (2018).

(35) Ma, W. C., Xie, S. J., Liu, T. T., Fan, Q. Y., Ye, J. Y., Sun, F. F., Jiang, Z., Zhang, Q. H., Cheng, J. & Wang, Y. Electrocatalytic reduction of CO_2 to ethylene and ethanol through hydrogen-assisted C–C coupling over fluorine-modified copper. *Nat. Catal*. **3**, 478–487 (2020) .

(36) Li, Z. L., Wang, J. J., Qu, Y. Z., Liu, H. L., Tang, C. Z., Miao, S., Feng, Z. C., An, H. Y. & Li, C. Highly selective conversion of carbon dioxide to lower olefins. *ACS Catal*. **7**, 8544−8548 (2017).

(37) Liu, X. L., Wang, M. H., Yin, H. R., Hu, J. T., Cheng, K., Kang, J. C., Zhang, Q. H. & Wang, Y. Tandem catalysis for hydrogenation of CO and CO_2 to lower olefins with bifunctional catalysts composed of spinel oxide and SAPO-34. *ACS Catal*. **10**, 8303−8314 (2020).

(38) Liu, X. L., Wang, M. H., Zhou, C., Zhou, W., Cheng, K., Kang, J. C., Zhang, Q. H., Deng, W. P. & Wang, Y. Selective transformation of carbon dioxide into lower olefins with a bifunctional catalyst composed of $ZnGa_2O_4$ and SAPO-34. *Chem. Commun*. **54**,

140−143 (2018).

(39) Gao, P., Dang, S. S., Li, S. G., Bu, X. N., Liu, Z. Y., Qiu, M. H., Yang, C. G., Wang, H., Zhong, L. S., Han, Y., Liu, Q., Wei, W. & Sun, Y. H. Direct production of lower olefins from CO_2 conversion via bifunctional catalysis. *ACS Catal*. **8**, 571−578 (2018).

(40) Su, J. J., Zhou, H. B., Liu, S., Wang, C. M., Jiao, W. Q., Wang, Y. D., Liu, C., Ye, Y. C., Zhang, L., Zhao, Y., Liu, H. X., Wang, D., Yang, W. M., Xie, Z. K. & He, M. Y. Syngas to light olefins conversion with high olefin/paraffin ratio using $ZnCrO_x$/AlPO-18 bifunctional catalysts. *Nat. Commun*. **10**, 1297 (2019).

(41) Wang, S., Zhang, L., Zhang, W. Y., Wang, P. F., Qin, Z. F., Yan, W. J., Dong, M., Li, J. F., Wang, J. G., He, L., Olsbye, U. & Fan, W. B. Selective conversion of CO_2 into propene and butene. *Chem* **6**, 3344–3363 (2020).

(42) Ni, Y. M., Chen, Z. Y., Fu, Y., Liu, Y., Zhu, W. L. & Liu, Z. M. Selective conversion of CO_2 and H_2 into aromatics. *Nat. Commun*. **9**, 3457 (2019).

(43) Li, Z. L., Qu, Y. Z., Wang, J. J., Liu, H. L., Li, M. R., Miao, S. & Li, C. Highly selective conversion of carbon dioxide to aromatics over tandem catalysts. *Joule*. **3**, 570–583 (2019).

(44) Sattler, J. J. H. B., Ruiz-Martinez, J., Santillan-Jimenez, E. & Weckhuysen, B. M. Catalytic dehydrogenation of light alkanes on metals and metal oxides. *Chem. Rev*. **114**, 10613–10653 (2014).

(45) Lu, P., Sun, J., Shen, D., Yang, R., Xing, C., Lu, C., Tsubaki, N. & Shan, S. Direct syngas conversion to liquefied petroleum gas: Importance of a multifunctional metal-zeolite interface. *Appl. Energ*. **209**, 1–7 (2018).

(46) Wang, K., Fan, S., Zhang, J., Ma, Q., Zhang, W. & Zhao, T. S. Effects of synergy between Cr_2O_3 and hierarchical HZSM-5 on transformation of LPG toward propylene and ethylene. *Fuel Process. Technol*. **179**, 53–59 (2018).

(47) Tong, M. L., Hondo, E., Chizema, L. G., Du, C., Ma, Q. X., Mo, S. T., Lu, C. X., Lu, P. & Tsubaki, N. Hydrogenation of CO_2 to LPG over CuZnZr/MeSAPO-34 catalysts. *New J. Chem*. **44**, 9328–9336 (2020).

(48) Liu, Z. P., Ni, Y. M., Sun, T. T., Zhu, W. L. & Liu, Z. M. Conversion of CO_2 and H_2 into propane over $InZrO_x$ and SSZ-13 composite catalyst. *J. Energy Chem*. **54**, 111–117 (2021).

(49) Li, C. M., Yuan, X. D. & Fujimoto, K. Direct synthesis of LPG from carbon dioxide over hybrid catalysts comprising modified methanol synthesis catalyst and -type zeolite. *Appl. Catal. A: Gen*. **475**, 155–160 (2014).

(50) Li, H. J., Zhang, P. P., Guo, L. S., He, Y. L., Zeng, Y., Thongkam, M., Natakaranakul, J., Kojima, T., Reubroycharoen, P., Vitidsant, T., Yang, G. H. & Tsubaki, N. Well-defined core-shell-structured capsule catalyst for direct conversion of CO_2 into liquefied petroleum gas. *ChemSusChem*. **13**, 2060–2065 (2020).

(51) Ramirez, A., Ticali, P., Salusso, D., Cordero-Lanzac, T., Ould-Chikh, S., Ahoba-Sam, C., Bugaev, A. L., Borfecchia, E., Morandi, S., Signorile, M., Bordiga, S., Gascon, J. & Olsbye, U. Multifunctional catalyst combination for the direct conversion of CO_2 to propane. *JACS Au* **1**, 1719–1732 (2021).

(52) Li, G., Jiao, F., Pan, X. L., Li, Na., Miao, D. Y., Li, L. & Bao, X. H. Role of SAPO-18 acidity in direct syngas conversion to light olefins. *ACS Catal*. **10**, 12370−12375

(2020).

(53) Lu, Z., Tracy, R. W., Abrams, M. L., Nicholls, N. L., Barger, P. T., Li, T., Stair, P. C., Dameron, A. A., Nicholas, C. P. & Marshall, C. L. Atomic layer deposition overcoating improves catalyst selectivity and longevity in propane dehydrogenation. *ACS Catal*. **10**, 13957−13967 (2020).

(54) Zhou, C. Q., Liu, K. W., Chen, X., Feng, J. H., Yang, J. L., Zhang, Z. Z., Liu, L., Xia, Y. & Shen, D. Z. Performance improvement of amorphous Ga_2O_3 ultraviolet photodetector by annealing under oxygen atmosphere. *J. Alloy. Compd*. **840**, 155585 (2020).

(55) Wang, J. J., Tang, C. Z., Li, G. N., Han, Z., Li, Z. L., Liu, H. L., Cheng, F. & Li, C. High-performance $MaZrO_x$ (Ma = Cd, Ga) solid-solution catalysts for CO_2 hydrogenation to methanol. *ACS Catal*. **9**, 10253−10259 (2019).

(56) Akkharaphatthawon, N., Chanlek, N., Cheng, C. K., Chareonpanich, M., Limtrakul, J. & Witoon, T. Tuning adsorption properties of $Ga_xIn_{2-x}O_3$ catalysts for enhancement of methanol synthesis activity from CO_2 hydrogenation at high reaction temperature. *Appl. Surf. Sci.* **489**, 278–286 (2019).

(57) Liang, F. L., Yu, Y., Zhou, W., Xu, X. Y. & Zhu, Z. H. Highly defective CeO_2 as a promoter for efficient and stable water oxidation. *J. Mater. Chem. A* **3**, 634–640 (2015).

(58) Jiang, X., Nie, X. W., Gong, Y. T., Moran, C. M., Wang, J. Y., Zhu, J., Chang, H. B., Guo, X. W., Walton, K. S. & Song, C. S. A combined experimental and DFT study of H_2O effect on In_2O_3/ZrO_2 catalyst for CO_2 hydrogenation to methanol. *J. Catal*. **383**,

283–296 (2020).

(59) Dang, S. S., Gao, P., Liu, Z. Y., Chen, X. Q., Yang, C. G., Wang, H., Zhong, L. S., Li, S. G. & Sun, Y. H. Role of zirconium in direct CO_2 hydrogenation to lower olefins on oxide/zeolite bifunctional catalysts. *J. Catal*. **364**, 382–393(2018).

(60) Kattel, S., Yan, B. H., Yang, Y. X., Chen, J. G. G. & Liu, P. Optimizing binding energies of key intermediates for CO_2 hydrogenation to methanol over oxide-supported copper. *J. Am. Chem. Soc*. **138**, 12440−12450 (2016).

(61) Yu, J. F., Yang, M., Zhang, J. X., Ge, Q. J., Zimina, A., Pruessmann, T., Zheng, L., Grunwaldt, J. D. & Sun, J. Stabilizing Cu^+ in Cu/SiO_2 catalysts with a shattuckite-like structure boosts CO_2 hydrogenation into methanol. *ACS Catal*. **10**, 14694−14706 (2020).

(62) Yao, L. B., Shen, X. C., Pan, Y. B. & Peng, Z. M. Synergy between active sites of Cu-In-Zr-O catalyst in CO2 hydrogenation to methanol. *J. Catal*. **372**, 74–85 (2019).

(63) Wang, Y. H., Kattel, S., Gao, W. G., Li, K. Z., Liu, P., Chen, J. G. G. & Wang, H. Exploring the ternary interactions in Cu-ZnO-ZrO_2 catalysts for efficient CO_2 hydrogenation to methanol. *Nat. Commun*. **10**, 1166 (2019).

(64) Yang, Y., Mims, C. A., Mei, D. H., Peden, C. H. F. & Campbell, C. T. Mechanistic studies of methanol synthesis over Cu from $CO/CO_2/H_2/H_2O$ mixtures: The source of C in methanol and the role of water. *J. Catal*. **298**, 10–17 (2013).

(65) Yan, B. H., Zhao, B. H., Kattel, S., Wu, Q. Y., Yao, S. Y., Su, D. & Chen, J. G. G. Tuning CO_2 hydrogenation selectivity via metal-oxide interfacial sites. *J. Catal*. **374**, 60–71 (2019).

(66) Feng, O. Y., Kondo, J. N., Maruya, K. & Domen, K. Site conversion of methoxy species on ZrO_2. *J. Phys. Chem. B* **101**, 4867–4869 (1997).

(67) Bjørgen, M., Svelle, S., Joensen, F., Nerlov, J., Kolboe, S., Bonino, F., Palumbo, L., Bordiga, S. & Olsbye, U. Conversion of methanol to hydrocarbons over zeolite H-ZSM-5: On the origin of the olefinic species. *J. Catal.* **249**, 195–207 (2007).

(68) Nieskens, D. L. S., Lunn, J. D. & Malek, A. Understanding the enhanced lifetime of SAPO-34 in a direct syngas-to-hydrocarbons process. *ACS Catal*. **9**, 691−700 (2019).

(69) Arora, S. S., Shi, Z. C. & Bhan, A. Mechanistic basis for effects of high-pressure H_2 cofeeds on methanol-to-hydrocarbons catalysis over zeolites. *ACS Catal*. **9**, 6407−6414 (2019).

(70) Wang, S., Chen, Y. Y., Wei, Z. H., Qin, Z. F., Ma, H., Dong, M., Li, J. F., Fan, W. B. & Wang, J. G. Polymethylbenzene or alkene cycle? Theoretical study on their contribution to the process of methanol to olefins over H-ZSM-5 zeolite. *J. Phys. Chem. C* **119**, 28482−28498 (2015).

(71) Deimund, M. A., Harrison, L., Lunn, J. D., Liu, Y., Malek, A., Shayib, R. & Davis, M. E. Effect of heteroatom concentration in SSZ-13 on the methanol-to-olefins reaction. *ACS Catal*. **6**, 542−550 (2016).

(72) Arora, S., Nieskens, D. L. S., Malek, A. & Bhan, A. Lifetime improvement in methanol-to-olefins catalysis over chabazite materials by high pressure H_2 co-feeds. *Nat. Catal*. **1**, 666–672 (2018).

(73) Zhao, X. B., Li, J. Z., Tian, P., Wang, L. Y., Li, X. F., Lin, S. F., Guo, X. W. & Liu, Z. M. Achieving a superlong lifetime in the zeolite-catalyzed MTO reaction under high

pressure: Synergistic effect of hydrogen and water. *ACS Catal*. **9**, 3017−3025 (2019).

Acknowledgements

The authors are grateful to the financial supports of the National Key R&D Program of China (2018YFB0604802), National Natural Science Foundation of China (U1910203; U1862101; 21991092; 21802157), Strategic Priority Research Program of the Chinese Academy of Sciences (CAS) (XDA21020500), Natural Science Foundation of Shanxi Province of China (201901D211581), Youth Innovation Promotion Association CAS (2021172), Autonomous research project of State Key Laboratory of Coal Conversion, Institute of Coal Chemistry, CAS (2020BWZ004), Young Talent Training Program of State Key Laboratory of Coal Conversion, Institute of Coal Chemistry, CAS (2021BWZ003), Excellent doctoral student award and subsidy program of Shanxi Province (BK2018001), East-West Cooperation Project of Ningxia Key R & D Plan (2017BY063), and the European Union's Horizon 2020 research and innovation program under grant agreement no 837733. The calculations were performed in the Computer Network Information Center of CAS and the National Supercomputer Centers in Lvliang of China.

Author contributions

S.W. implemented the experiments including catalyst preparation, characterization, catalytic reaction and theoretical calculation, and wrote the paper; L.Z., P.W., W.J., Z.Q., M.D. carried out part of catalytic tests, theoretical calculation as well as some catalyst characterizations;

J.W., U.O. gave fruitful discussions on the reaction mechanism; W.F. conceived the whole project, guided the work and revised the paper. All the authors contributed to the discussions on the experimental and theoretical calculation results.

Additional information

Supplementary Information accompanies this paper at http://www.nature.com/nature communications.

Competing Interests: The authors declare no competing interests.

Figure 1.

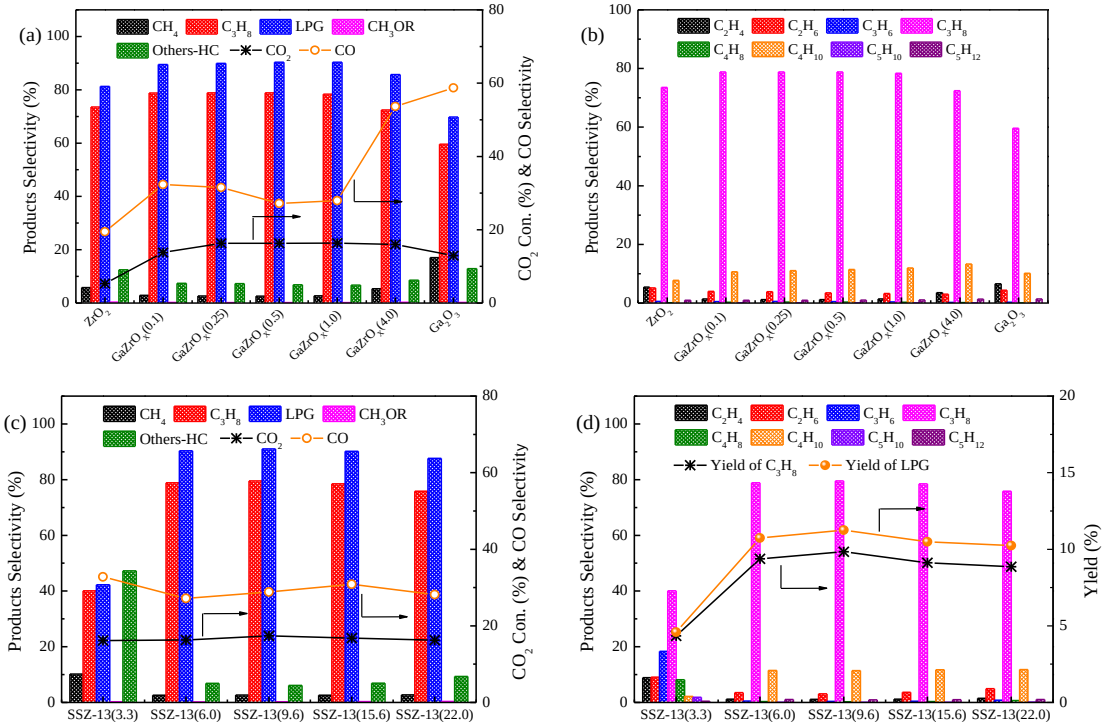

Figure 1. (a) and (b) the catalytic performance for direct conversion of CO_2 into propane over various $GaZrO_x$(N) and H-SSZ-13(6.0) catalysts; (c) and (d) influence of the Si/Al ratio of H-SSZ-13 zeolite on the CO_2 conversion and product distribution in direct hydrogenation of CO_2 into propane over various $GaZrO_x$(0.5)/H-SSZ-13 catalysts. Others-HC represents the selectivity of hydrocarbons, excluding the methane, propane and butane. The CH_3OR (R = H or CH_3) is sum of methanol and dimethyl ether. Typical reaction conditions: H_2/CO_2 = 3:1, GHSV = 2400 mL/(g·h), 3.0 MPa and 350 °C.

Figure 2.

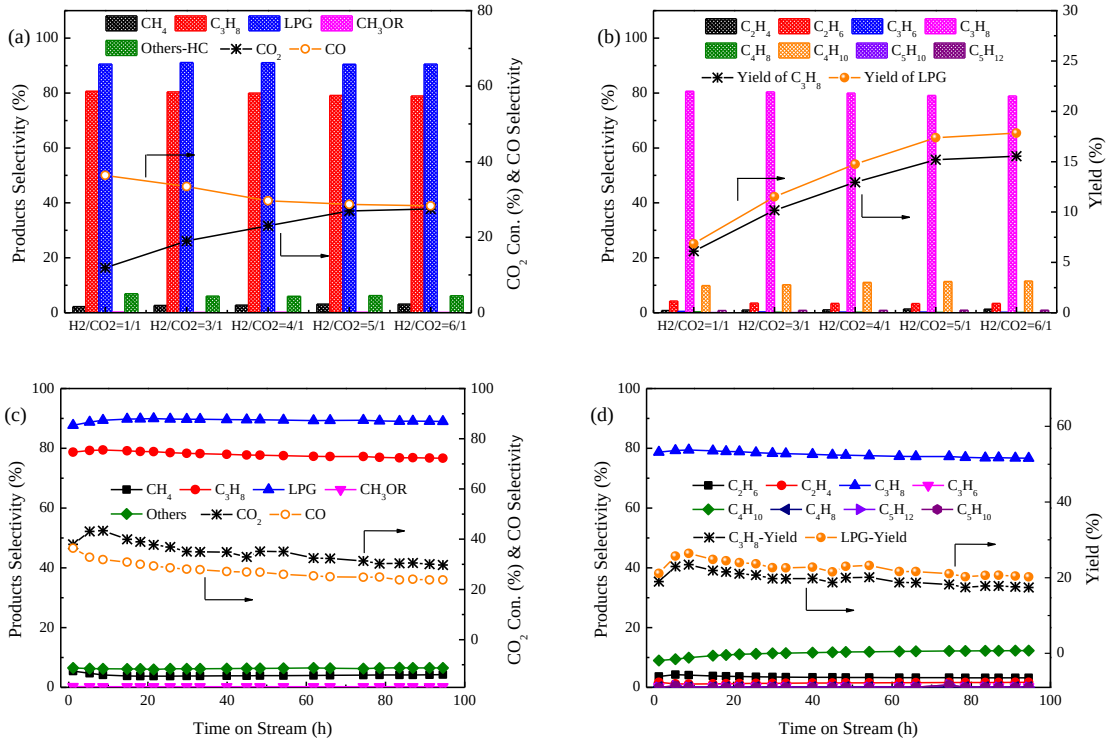

Figure 2. (a) and (b) the influence of H_2/CO_2 ratio on the catalytic performance for direct conversion of CO_2 into propane over $GaZrO_x(0.5)$/H-SSZ-13(6.0) catalyst at 3.0 MPa, 350 °C and GHSV = 1200 mL/(g·h); (c) and (d) evolution of CO_2 conversion and product distribution with reaction time over $GaZrO_x(0.5)$/H-SSZ-13(6.0) catalyst (reaction conditions: H_2/CO_2 = 6/1, 350 °C, 3.0 MPa and GHSV = 960 mL/g·h). Others-HC represents the selectivity of hydrocarbons, excluding the methane, propane and butane. The CH_3OR (R = H or CH_3) is sum of methanol and dimethyl ether.

Figure 3.

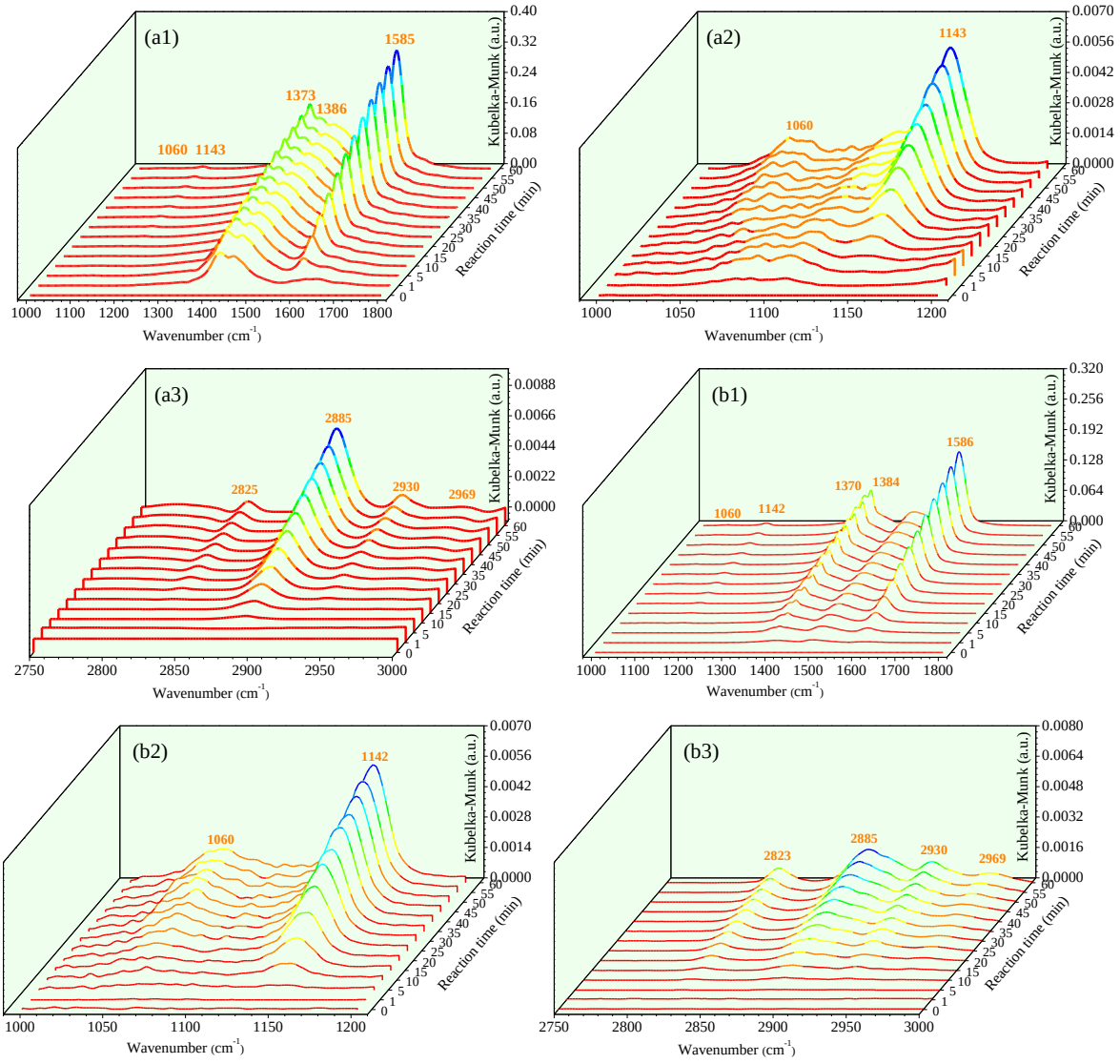

Figure 3. Time-dependent DRIFT spectra for CO_2 hydrogenation to methanol on the $GaZrO_x(0.5)$ (a) and $GaZrO_x(4.0)$ (b) oxides. The spectra was collected every 5 min up to 60 min after pre-treatment of the sample with H_2 (30 mL/min) for 2 h at 400 °C and purged with Ar (30 mL/min) for 0.5 h at 300 °C (Typical reaction conditions: 300 °C and 0.1 MPa).

Figure 4.

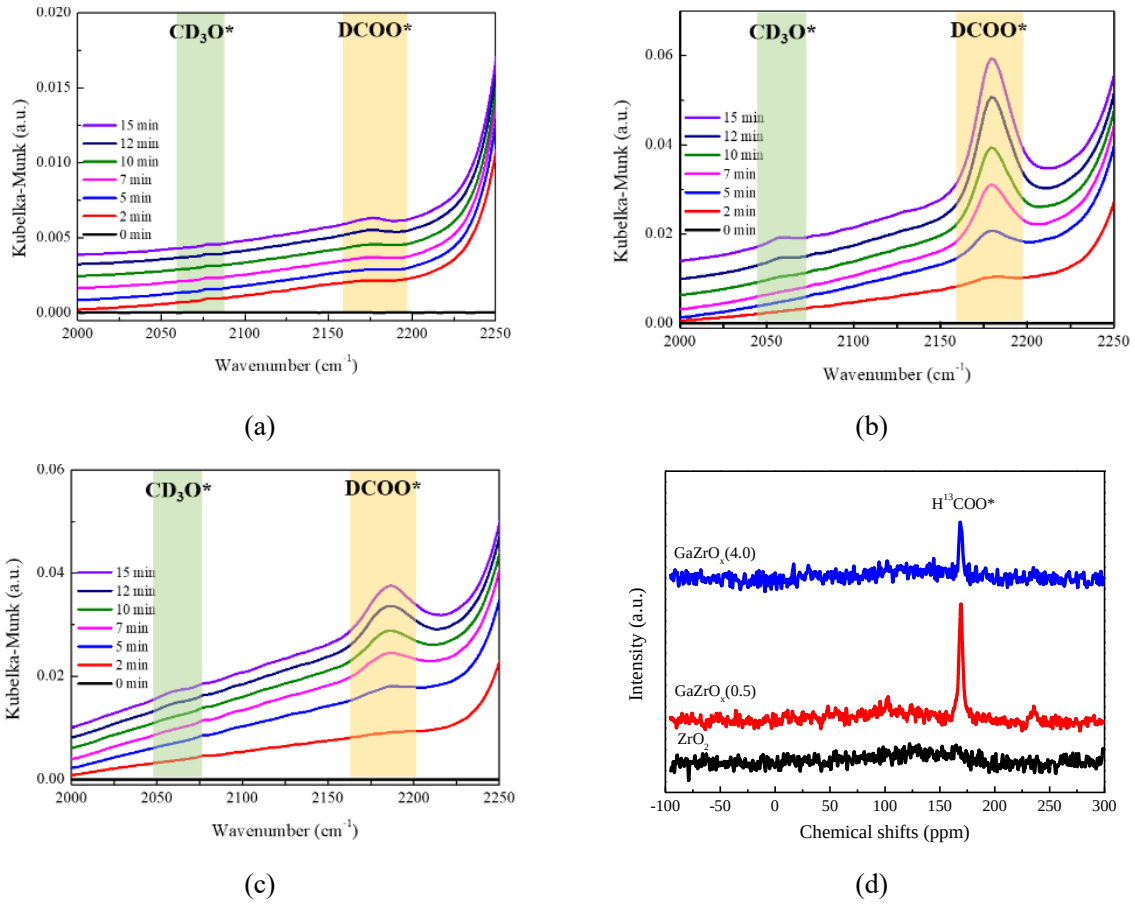

Figure 4. Time-dependent DRIFT spectra for CO_2 + D_2 reaction on ZrO_2 (a), $GaZrO_x$(0.5) (b) and $GaZrO_x$(4.0) (c) oxides at 300 °C, as collected at a resolution of 4 cm^{-1} by accumulating 64 scans. ^{13}C MAS NMR spectra (d) for converting $^{13}CO_2$ and H_2 on ZrO_2, $GaZrO_x$(0.5) and $GaZrO_x$(4.0) oxides at 300 °C.

Figure 5.

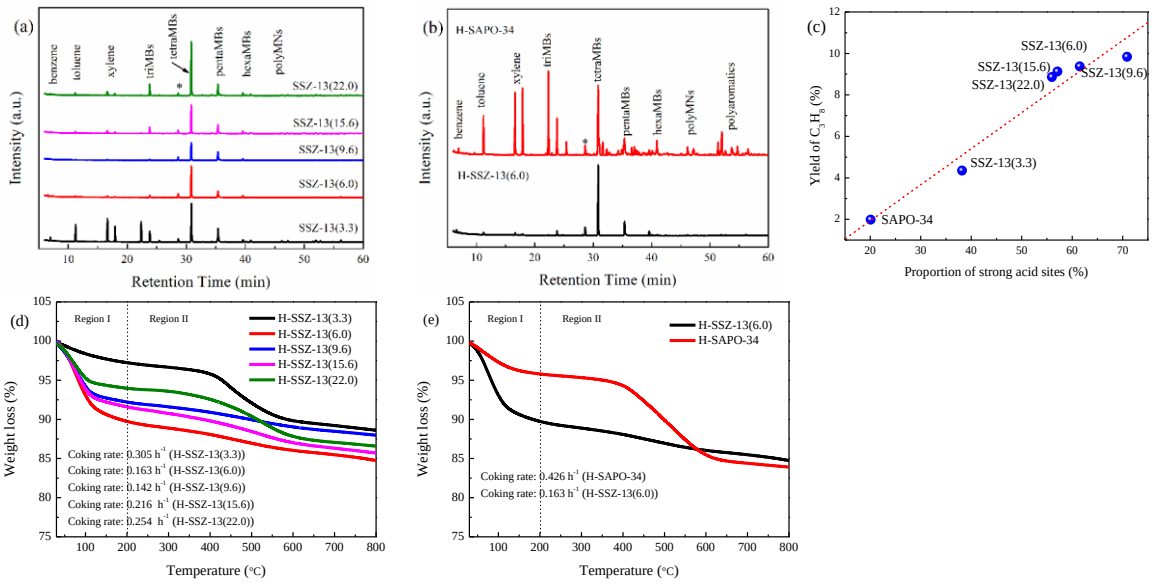

Figure 5. (a) and (b) GC-MS diagrams of the carbonaceous species confined in the $GaZrO_x(0.5)$/H-SSZ-13 and $GaZrO_x(0.5)$/H-SAPO-34 catalysts after catalyzing CO_2 conversion into propane around 30 h. * is the internal standard (hexachloroethane); (c) the relation of propane yield with the proportion of strong acid sites of H-SSZ-13 and H-SAPO-34 zeolites. The proportion of strong acid sites is obtained from the results of NH_3-IR. (d) and (e) TG curve of $GaZrO_x(0.5)$/H-SSZ-13 and $GaZrO_x(0.5)$/H-SAPO-34 catalysts after catalyzing the CO_2 hydrogenation to propane for around 30 h (The data represent the coking rate (h^{-1}) at >200 ºC).

Figure 6.

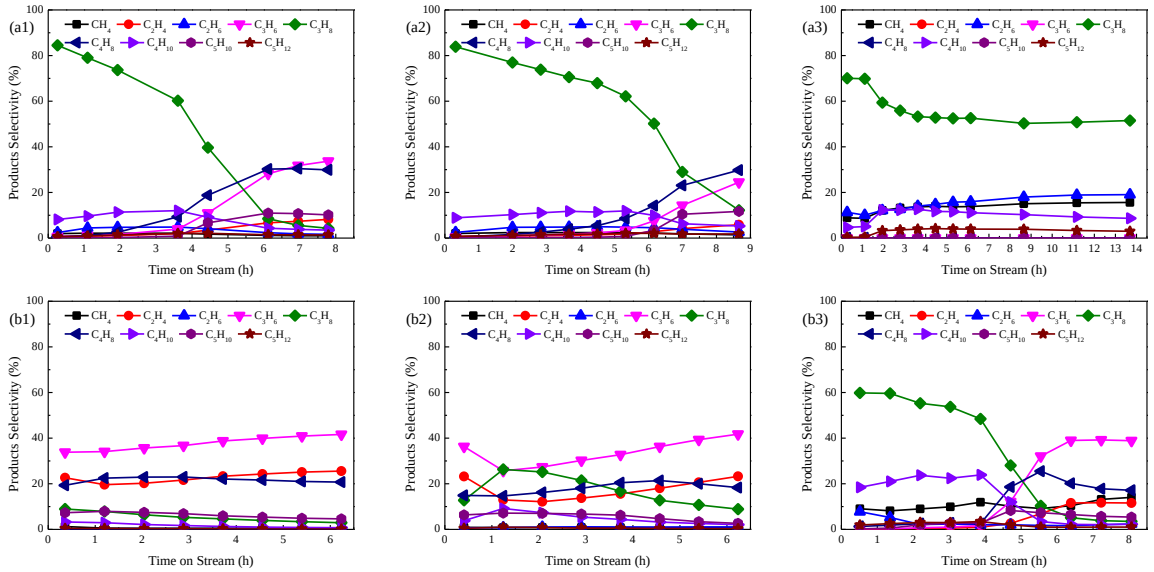

Figure 6. The catalytic performance of methanol conversion over H-SSZ-13 zeolite (a) under Ar atmosphere at 0.1 MPa (1) and H_2 atmosphere at 0.1 MPa (2) and 3.0 MPa (3), and H-SAPO-34 zeolite (b) under Ar atmosphere at 0.1 MPa (1) and H_2 atmosphere at 0.1 MPa (2) and 3.0 MPa (3). Typical reaction conditions: 350 °C and $WHSV_{methanol}$ of 0.24 h^{-1}.

Figure 7.

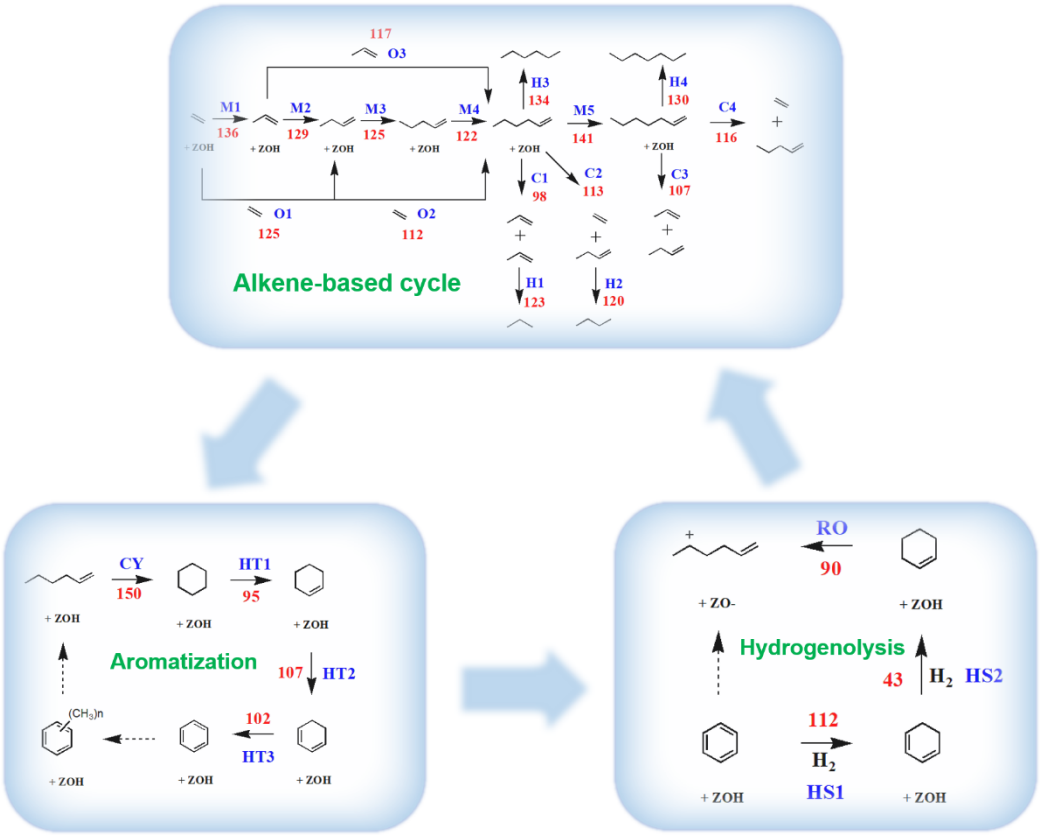

Figure 7. Reaction network and calculated intrinsic kinetics of various elemental steps for alkene-based cycle, aromatization and hydrogenolysis reactions over H-SSZ-13. The data represent the free energy barrier (kJ mol^{-1}). M, O, C, H, CY, HT, HS and RO are short for methylation, oligomerization, cracking, hydrogenation, cyclization, hydride transfer, hydrogenolysis and ring-opening reactions, respectively.

Figure 8.

Figure 8. Reaction scheme for direct conversion of CO_2 into propane over $GaZrO_x$/H-SSZ-13 catalyst system.